Acoustic modeling of micro-lattices obtained by additive manufacturing

Jean Boulvert, Josué Costa-Baptista, Théo Cavalieri, Maxime Perna, Edith
Roland Fotsing, Vicente Romero-García, Gwenael Gabard, Annie Ross, Jacky
Mardjono, Jean-Philippe Groby

Acoustic modeling of micro-lattices obtained by additive manufacturing

Jean Boulvert,[1,2,3,a)] Josué Costa-Baptista,[1] Théo Cavalieri,[2,3] Maxime Perna,[1] Edith Roland Fotsing,[1] Vicente Romero-García,[2] Gwénaël Gabard,[2] Annie Ross,[1,b)] Jacky Mardjono,[3,c)] and Jean-Philippe Groby[2,d)]

[1)]*Laboratoire d'Analyse Vibratoire et Acoustique, LAVA, Mechanical engineering, Polytechnique Montréal, Montréal, Québec, Canada*
[2)]*Laboratoire d'Acoustique de l'Université du Mans, LAUM - UMR CNRS 6613, Le Mans Université, Avenue Olivier Messiaen, 72085 Le Mans Cedex 9, France*
[3)]*Safran Aircraft Engines, Villaroche, Rond Point René Ravaud - Réau, 77550 Moisy-Cramayel Cedex, France*

(Dated: July 8, 2019)

The acoustic behavior of 3D printed micro-lattices is investigated to assess the impact of defects induced by the Fused Deposition Modeling technique on the parameters of the equivalent fluid medium. It is shown that manufacturing process leads to three types of non-trivial defects: elliptical filament sections, pinch and filaments surface rugosity. Not considering these defects may lead to important acoustic predictions errors. Inverse characterization of three samples allows to fit the acoustic prediction model considering this kind of defects.

I. INTRODUCTION

Additive manufacturing has proved to be a versatile and promising tool to produce sound absorbing materials. Helmholtz resonators[1], straight[2], inclined[3] and coiled tubes[1], sonic crystals[4] , micro perforated panels[5] and porous treatments such as micro-lattices[6–8] are among some intersting applications. For all these acoustic materials, simple analytical models can be used to describe, analyze and optimize the geometry. Numerical or analytical models[9,10] showed that the acoustical parameters of the porous material strongly depend on several geometrical parameters of the micro-structure and can be strongly affected by the manufacturing, such as change in the filaments shape of micro-lattice[11], presence of sinusoidal rugosity in micro slits[12], and surface irregularities in packed micro tubes[13]. Therefore, the impact of additive manufacturing imprecision on acoustic parameters could be very important and needs to be well described. Usually discrepancies between models and experimental data are ascribed to the additive manufacturing inaccuracy or its inability to reproduce an idealized geometry[14,15].

In this work a combined numerical and experimental approach is used to describe the differences between a 3D printed micro-lattice and its idealized representation in terms of the geometry and the acoustic response. The 3D printed micro-lattices can be acoustically described by the Johnson-Champoux-Allard-Lafarge (JCAL) model[16] which accounts for the thermal and viscous losses in the effective bulk modulus and density, respectively. They are expressed in terms of air parameters and six parameters depending on the micro structure of the porous medium. These JCAL parameters can be obtained by applying inverse characterization techniques from the measurements of the scattering coefficients of a layer of porous material. In particular, the method proposed by Niskanen et al[17] can be used. This method is based on a statistical inversion using Bayes' formula and does not require any previous knowledge on the sample except its thickness. Moreover, in the particular case where a Representative Elementary Volume (REV) having a subwavelength scale dimension can be defined, these JCAL parameters can be also numerically computed using the Multi-Scale Asymptotic Method (MAM)[9]. In the case of periodic porous medium such as micro-lattices, the REV is the constitutive unit cell (an elementary periodic volume). Through these two techniques the effects of the manufacturing defects on the acoustic response of the 3D printed material were analyzed. The methodology presented in this paper can be extended to other 3D printed porous materials of different micro structure or manufacturing process.

The article is organized as follows: first the micro-lattice fabrication is presented. The additive manufacturing procedure, creating the microstructure governing the material acoustic behavior, is detailed. Then, the corresponding expected and actual micro-lattice is analyzed. The discrepancies are identified in terms of micro-geometry differences. In the second part, the acoustic simulation and experimental characterization procedures are explained. Finally, the acoustic impact of the additive manufacturing defects is analyzed. This last section exposes the procedure that must be applied in order to obtain an accurate acoustic prediction model.

[a)]jean.boulvert@univ-lemans.fr;
[b)]annie.ross@polymtl.ca
[c)]jacky.mardjono@safrangroup.com
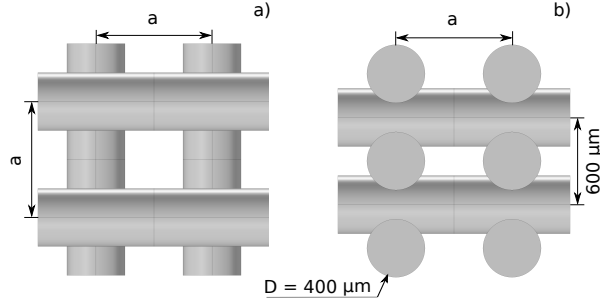[d)]jean-philippe.groby@univ-lemans.fr

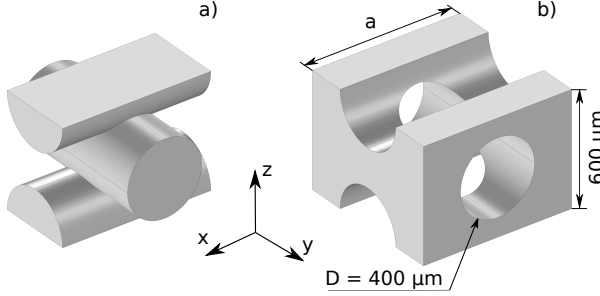Figure 1. Idealized geometry. a) Top view. b) Cross section.

Figure 2. Idealized Representative Elementary Volume. a) Solid phase b) Fluide phase.

II. IDENTIFICATION OF THE MANUFACTURING DEFECTS

In this section, the manufacturing process and the expected resulting micro-lattice are described. Then, the manufacturing induced defects are analyzed on the basis of geometrical observations.

A. Additive manufacturing procedure

The Fused Deposition Modeling (FDM) *Pro2* printer supplied by *RAISE3D* was used to produce 30 mm thick, cylindrical samples with a diameter of 30 mm. The extruded material is polylactic acid (PLA). The diameter of the nozzle is $D_n = 400\,\mu$m. The revolution axis of the sample is placed vertically. The nozzle temperature is set to 210°C, its displacement speed to 40 mm/s and the extrusion multiplier to 1.

The samples were printed in orthogonal direct configuration: a given micro-layer is made of parallel rods; the next micro-layer of parallel rods is orthogonal to the previous layer. This configuration is also known as "woodpile" or "interwoven perpendicular arrangement". The printer's nozzle extrudes a rods layer in the horizontal plane, then the build plate shifts vertically and allows the next orthogonal layer to be printed. The build plate displacement is set to $300\,\mu$m. In this way, two consecutive orthogonal layers are separated by
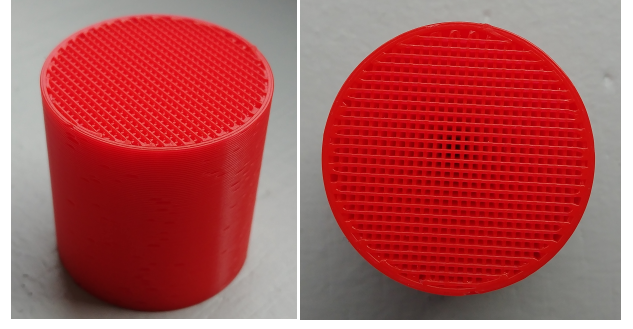

Figure 3. Pictures of homogeneous sample.

$300\,\mu$m and two consecutive parallel layers are separated by $600\,\mu$m. Since the filaments' diameter, D, is close to D_n, the contact between two layers is substantial as it can be seen in the idealized geometry shown in Fig. 1.

The in-plane spacing between the filaments, i.e. the lattice constant of the micro-lattice, a, can also vary. A normalized lattice parameter is defined as $A = a/D$ ($A \geq 1$). Samples are homogeneous if A is kept constant trough the sample's thickness, or multilayered if A varies through the thickness. An intuitive representation of the micro-lattice would be a superposition of perfectly cylindrical parallel rods, alternating orthogonal in plane directions, each layer spaced by $300\,\mu$m from one another (Fig. 1). The rods diameter would be equal to the nozzle diameter: $D = D_n$.

Two pictures of a representative homogeneous sample are presented in Fig. 3. To the naked eye, the printed geometry is consistent with the idealized one. The filaments seem to be well aligned and no macroscopic defect is identifiable. It is worth noting that a $800\,\mu$m thick solid layer surrounds the porous micro-lattice to provide consistency.

B. Idealized Representative Elementary Volume

From the idealized geometry (Fig. 1), an indivisible periodic pattern, called "unit cell", can be extracted. The considered idealized unit cell is represented in Fig. 2. In the homogenization theory[9], as the porous medium is structured, the unit cell plays the role of the "Representative Elementary Volume" (REV). More details are given below on how this theory is used to predict a porous material's acoustic behavior.

C. Manufacturing geometry inherent defects

The printed samples were analyzed by means of optical microscope and scanning electron microscope (SEM) in order to identify the different possible manufacturing geometrical defects. The optical microscope has a
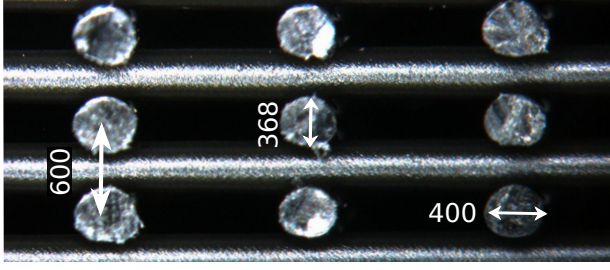
Figure 4. Microscopic image of a micro-lattice cross section. Dimensions in micrometers.

Figure 5. Microscopic images of micro-lattices, tope view. ED arrows indicate the extrusion direction. Dimensions in micrometers.

$64\times$ zoom and is equipped with a digital camera for the pictures acquisition. The SEM produces images of the sample's surface in two dimensions (i.e. the depth of the surfaces irregularities cannot be assessed). The accuracy of SEM enables to distinguish details smaller than $1\,\mu$m. Samples were not coated since their conductivity was high enough to obtain high-quality images. Three defects were identified.

1. Filaments elliptical section

Figure 4 shows an image obtained from the optical microscope of a manually sliced sample. The image reveals two important observations. The first one is that the filament section is not perfectly circular but rather elliptical with an horizontal major axis. The flattening of the micro-rods depends on the printing parameters. In our case the minor axis represents in average, 92% of the major axis leading to filaments width equals to the nozzle diameter in the horizontal direction (400 μm) and 92% of the nozzle diameter (368 μm) in the vertical direction. This defect does not depend on the filaments spacing. The second important observation is that the spacing between two consecutive orthogonal layers is respected and is equal to $300\,\mu$m.

2. Filaments section pinch

Due to the extrusion process, the filaments are subjected to a section pinch phenomenon. The filament is extruded by the printer then pulled by its nozzle following a given trajectory and enters in contact with the previous layer only at the junctions. Between two junctions the pinch is clearly identifiable as shown in Fig. 5. In fact, the section of the filaments decreases between two consecutive junctions in the direction of the material deposition. Figure 5 shows that the widths $D1$ and $D1'$ are smaller than $D2$ and $D2$', respectively. Empirical laws have been derived to describe the minimum filament width (MFW) and its position (MFWP), in micrometers, as a function of the filaments step and nozzle diameter, in micrometers:
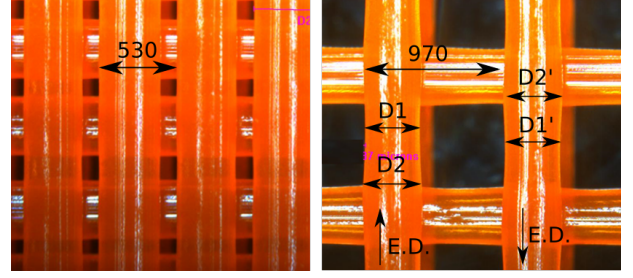
$$\text{MFWP} = D_n(0.8A - 1), A \in [1.5; 11] \tag{1}$$

$$\text{MFW} = \frac{287 D_n A + 1.414 \times 10^6}{D_n A + 3391}, A \in [2; 11]. \tag{2}$$

These laws have been derived based on the microscope measurement of 10 samples with A ranged between 1.5 and 11. The measurement of MFW is only satisfactory when A is higher than 2. Below this spacing, the pinch is too small to be correctly measured.

3. Filaments micro grooves

The bright lines appearing on microscopic images of micro-lattice (see Fig. 5) brought the attention to the nano-scale defects. The surfaces of the micro-rods are not perfectly smooth. Figure 6 shows the image of a SEM analysis revealing impurities scattered all over the filament surface. Moreover, many nano-grooves are clearly identifiable. These grooves are aligned with the filament direction. Their width ranges between 5 and $20\,\mu$m. However, their exact distribution and depth could not be evaluated by the SEM. A simple explanation of the grooves origin would be that the printer nozzle's inner surface is not smooth. As a consequence, this defect might be specific to the printer nozzle.

III. ACOUSTIC SIMULATION AND EXPERIMENTAL CHARACTERIZATION

A. Modeling procedure

In order to assess the impact of each defect separately, a modeling procedure is implemented. It considers the acoustic wave propagation in homogeneous and multi-layer porous media as a function of microscopic parameters computed by a numerical method.
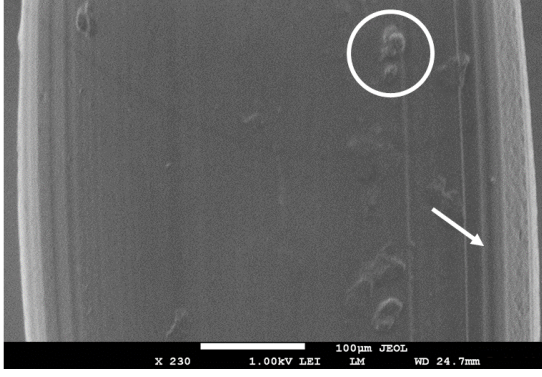
Figure 6. SEM image of the micro-lattice, plane vue. The circle indicates an impurity, the arrow indicates a nano-groove.

1. Acoustic model for porous media

The energy of acoustic waves penetrating a porous medium is dissipated mainly through the interaction of the wave between the frame and the pore saturating fluid (in our case air) resulting in viscous and thermal losses. If the skeleton is sufficiently dense and rigid, it can be decoupled from the air. Then, the porous medium can be considered as an equivalent fluid characterized by its complex and frequency dependent effective bulk modulus K_{eq} and density ρ_{eq}. The properties of the equivalent fluid depend on the microstructure of the porous medium and govern its acoustic behavior[18]. There are three options to predict the properties of porous media's equivalent fluid. The first one consists in using empirical laws correlating few parameters[18]. However, these laws only apply to small ranges of materials, similar to each other. The second option can be applied if the porous medium is made of aligned, non-crossing cylindrical micro-rods[4]. For this precise case, the porous material is named "sonic crystal" and an analytical solution has been derived for porosity larger than 0.7. The last, is a semi-empirical approach[18]. This kind of model is not limited to a few applications but requires more parameters than empirical or analytical laws. This is the case of the JCAL model[16] that provides the expression of the density and bulk modulus of the porous material as follows,

$$\rho_{eq}(\omega) = \frac{\rho_0}{\phi}\alpha(\omega), \qquad (3)$$

$$K_{eq}(\omega) = \frac{\gamma P_0}{\phi}\left(\gamma - \frac{\gamma-1}{\alpha'(\omega)}\right)^{-1}, \qquad (4)$$

where ω is the angular frequency, ρ_0 the density of the saturating fluid, i.e. the air medium, P_0 the static pressure, γ the specific heat ratio, ϕ the porous material porosity, $\alpha(\omega)$ its dynamic tortuosity, and $\alpha'(\omega)$ its ther-

mal tortuosity. The latters are defined as

$$\alpha(\omega) = \alpha_\infty - \frac{i\nu}{\omega}\frac{\phi}{q_0}\sqrt{1 + \frac{i\omega}{\nu}\left(\frac{2\alpha_\infty q_0}{\phi\Lambda}\right)^2}, \qquad (5)$$

$$\alpha'(\omega) = 1 - \frac{i\nu'}{\omega}\frac{\phi}{q_0'}\sqrt{1 + \frac{i\omega}{\nu'}\left(\frac{2q_0'}{\phi\Lambda'}\right)^2}, \qquad (6)$$

where $\nu = \eta/\rho_0$ is the kinematic viscosity of the saturating fluid, η its dynamic viscosity, $\nu' = \nu/Pr$, Pr the Prandtl number, α_∞ the porous material geometrical tortuosity, Λ its viscous characteristic length, Λ' its thermal characteristic length, q_0 its visco-static permeability and q_0' its thermo-static permeability.

Once the equivalent fluid parameters are known, the acoustic behavior of the considered porous medium can be predicted. The equivalent fluid wave number k_{eq} and characteristic impedance Z_{eq} take the form:

$$k_{eq} = \omega\sqrt{\frac{\rho_{eq}}{K_{eq}}}, \qquad (7)$$

$$Z_{eq} = \sqrt{\rho_{eq}K_{eq}}, \qquad (8)$$

The acoustic behavior of a porous medium is then described by its six JCAL parameters: ϕ, α_∞, Λ, Λ', q_0 and q_0'.

2. Transfer Matrix Method

The Transfer Matrix Method (TMM) is a well-known method used to predict the acoustic behavior of a multilayer (or monolayer) sound absorber[18]. The transfer matrix of a porous layer is expressed in terms of its thickness, equivalent fluid wave number and characteristic impedance. The total transfer matrix of a multilayer is the product of the slabs' matrices and leads to the surface impedance Z_s of the multilayer. The sound absorption coefficient $\mathcal{A}$ of a multilayer can be calculated by:

$$\mathcal{A} = 1 - \left|\frac{Z_s - Z_0}{Z_s + Z_0}\right|^2, \qquad (9)$$

where Z_0 is the acoustic impedance of the air. As stated above, the porous samples are framed by a thin solid ring. Its effect is considered by correcting the surface impedance by the ratio S_{sample}/S_{porous}[18] in Eq. (9).

$$Z_{s^*} = Z_s\frac{S_{sample}}{S_{porous}}. \qquad (10)$$

The radiation effect of the solid ring is negligible.

3. Porous media: Multi-Scale Asymptotic Method

In this work MAM[9] was used to numerically evaluate the JCAL parameters of a porous material made from

4

the idealized REV. This method solves fundamental equations in the REV's fluid domain and then computes the JCAL parameters. The MAM can be implemented in a Finite Element Method (FEM) code from which the JCAL parameters are computed for any open-cell respecting the scales separation[10]. It is a well suited method for the numerical evaluation of micro-geometry defects because they can be controlled and considered separately or simultaneously.

The MAM has been implemented in the commercial FEM software *Comsol Multiphysics*. Three problems (Eqs. 11, 12, 13) are solved in order to retrieve the six JCAL parameters defining the porous medium's equivalent fluid when the pressure wave travels in the **z** direction (Fig. 2). The thermal problem equation, taking the limit in $\omega \to 0$, reads

$$\begin{cases} \mathrm{div}(\mathbf{grad}(\theta)) = -1, \\ \theta = 0 \text{ on } \Gamma_{fs}, \\ \theta \ \Omega\text{-periodic}, \end{cases} \quad (11)$$

where Γ_{fs} is the fluid solid interface and Ω the REV. The visco-interial problem, taking the limit in $\omega \to 0$, is

$$\begin{cases} \mathrm{div}(\mathbf{grad}(k_z^0)) = \frac{\partial \xi_j^0}{\partial z} - 1, \\ \frac{\partial k_z^0}{\partial z} = 0, \\ k_z^0 = 0 \text{ on } \Gamma_{fs}, \\ \langle k_z^0 \rangle_{\Omega} = 0, \\ k_z^0 \text{ and } \xi^0 \ \Omega\text{-periodic}, \end{cases} \quad (12)$$

where $\langle \cdot \rangle_{\Omega}$ is the REV averaging. The visco-interial problem, taking the limit in $\omega \to \infty$, becomes

$$\begin{cases} \frac{i\omega\rho_0}{\eta} k_z^{\infty} = \frac{\partial \xi_z^{\infty}}{\partial z} - 1, \\ \frac{\partial k_z^{\infty}}{\partial z} = 0, \\ k_z^{\infty} \cdot \mathbf{n} = 0 \text{ on } \Gamma_{fs}, \\ \langle \xi_z^{\infty} \rangle_{\Omega} = 0, \\ k_z^{\infty} \text{ and } \xi_z^{\infty} \ \Omega\text{-periodic}, \end{cases} \quad (13)$$

where **n** is the solid surface normal vector.

The JCAL parameters are obtained by integrating, over the fluid domain Ω_f or fluid-solid interface Γ_{fs}, the solution fields of these equations. They are expressed as

$$\phi = \frac{\int_{\Omega_f} d\Omega_f}{\int_{\Omega} d\Omega}, \qquad \alpha_{\infty} = \phi \langle 1 - \frac{\partial \xi_z^{\infty}}{\partial z} \rangle^{-1},$$
$$\Lambda = 2 \frac{\int_{\Omega_f} k_z^{\infty} \cdot k_z^{\infty} d\Omega_f}{\int_{\Gamma_{fs}} k_z^{\infty} \cdot k_z^{\infty} d\Gamma_{fs}}, \qquad \Lambda' = 2 \frac{\int_{\Omega_f} d\Omega_f}{\int_{\Gamma_{fs}} d\Gamma_{fs}},$$
$$q_0 = \langle k_z^0 \rangle_{\Omega}, \qquad q_0' = \frac{\int_{\Omega_f} \theta d\Omega_f}{\int_{\Omega_f} d\Omega_f}.$$

B. Acoustic experimental characterization

The acoustic impact of the geometry defects can be assessed numerically by means of the MAM. As a complement to this numerical approach, the samples were also characterized by experimental acoustic techniques.

1. Acoustic direct characterization

The acoustic scattering parameters of the considered samples were measured using a 30 mm diameter impedance tube following the ASTM E1050 and ISO 10534-2 standards. The absorption coefficients were measured using the two microphones technique with hard backing configuration. The data required for the inverse characterizations (see below) were obtained using the four microphones technique with an anechoic termination. The measurements were made between 500 Hz and 6500 Hz.
Homogeneous samples were measured in both direct and reverse orientations to make sure they are symmetric and thus, most probably homogeneous. Every sample was measured three times in both orientations. For each measurement, the sample was removed and installed again in the tube. Regardless of the measurement orientation, the absorption curves were always superimposed.

2. Acoustic inverse characterization

While the MAM can be used to compute the JCAL parameters from a REV description, the measured of reflection and transmission coefficients of an homogeneous porous slab can be used to recover its JCAL parameters. Diverse methods have been discussed in the literature; in the present work, the inverse method proposed by Niskanen et al[17] is used. To perform the procedure, the sample of interest is tested in a four microphones impedance tube to measure the reflection coefficient on both sides along with the transmission coefficient. During the inversion, the JCAL parameters are bounded to realistic values (eg. $\phi \in [0; 1]$) and forced to respect the natural physical conditions $\Lambda \leq \Lambda'$ and $q_0 \leq q_0'$. In some cases, the reflection and transmission coefficients are strongly correlated to a subset of JCAL parameters while the other ones have a small impact. Then, the precise inverse characterization of the JCAL parameters is complicated. Adjusting the parameters bounds to account for their prior knowledge, obtained from the numerical model, limits the field of inverse characterization research and leads to more accurate values. In this way, the retrieved JCAL parameters follow realistic trends, as function of the filament spacing.

IV. EFFECT OF MANUFACTURING DEFECTS ON THE JCAL PARAMETERS: NUMERICAL EVALUATION

Three additive manufacturing inherent defects have been identified. Their impact on the acoustic response depends on the spacing of the rods. In this section, their impact is studied for the range of $A \in [1.2; 25]$.
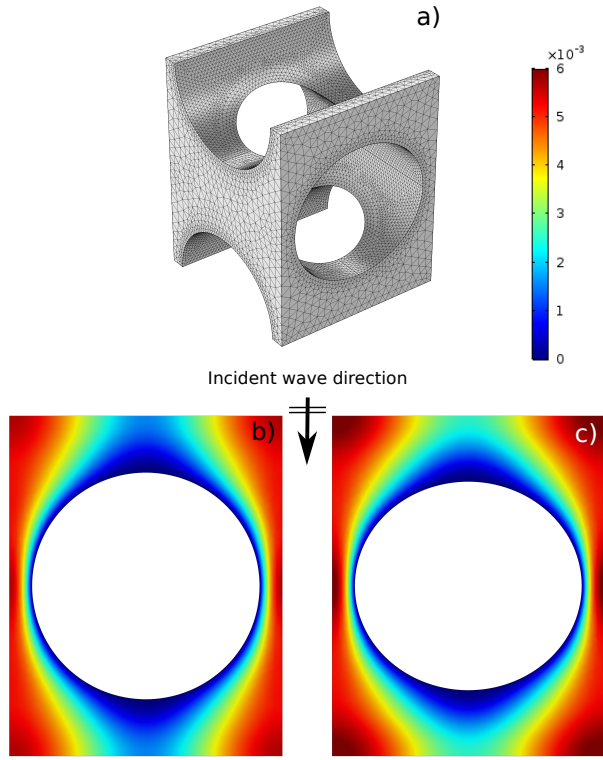
Figure 7. 3D micro-lattice MAM visco-static simulation with $A = 1.2$. a) Unit cell. b) Incident wave direction velocity field's component with cylindrical rods. c) Incident wave direction velocity field's component with elliptical rods. The minor vertical axis is equal to 92% of the major horizontal one.

A. Elliptical section and section pich

The impact of the elliptical section and pinch of the filaments are analyzed in this section by modifying the idealized REV. The micro-lattice composed of perfectly cylindrical rods is taken as a reference. The considered elliptical section has a $368\,\mu m$ vertical minor axis and a $400\,\mu m$ horizontal major axis. The geometry of the pinch is described by Eqs. (1) and (2). Figure 7(a) shows the meshed REV used in these calculations. An example of the visco-static MAM field is given in Figs. 7(b) and (c) for the case of perfectly cylindrical and elliptical rods, respectively. This field is used to compute the viscous permeability q_0.

The section pinch is considered ineffectual when A is lower than 2 and is not accounted for in the unit cell. The defects impacts are summarized on Table I with the following main findings:

- the elliptical filament section significantly increases the porosity ϕ and permeabilities q_0 and q_0' when the filaments are very close to each other and slightly increases the thermal length Λ';

Table I. JCAL parameters relative difference (%) with respect to perfectly cylindrical rods.

Defect	A	ϕ	α_∞	Λ	Λ'	q_0	q_0'
	1.2	15	2	0	5	19	22
Elliptical	10	1	0	0	4	3	1
	25	0	0	0	4	2	0
Pinch	10	1	0	1	9	4	5
	25	1	1	0	12	2	2
Elliptical	1.2	15	2	0	5	19	21
and	10	2	0	1	13	5	6
Pinch	25	1	0	0	17	2	3

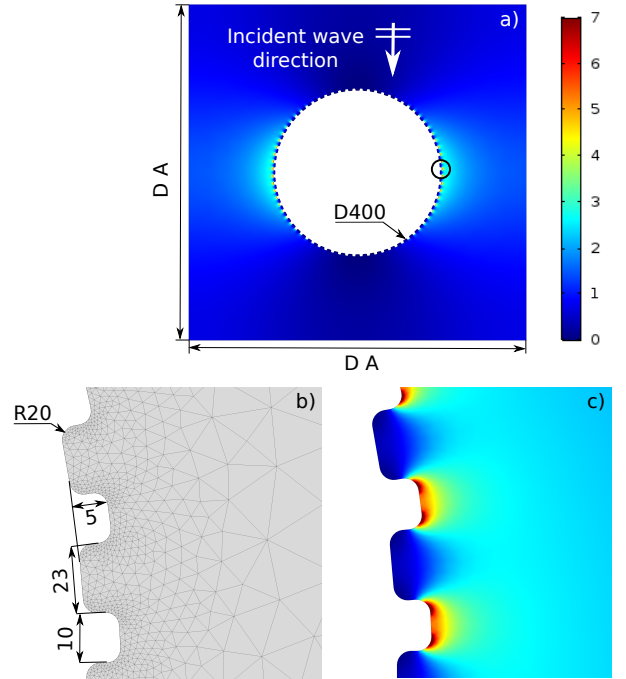
Figure 8. Grooved filament MAM simulation. a) Considered unit cell and visco-inertial, $\omega \to \infty$, MAM velocity field. b) Grooves geometry and mesh. c) Visco-inertial, $\omega \to \infty$, MAM velocity field detail. All dimensions are in micro meters.

- the filament section pinch increases the thermal length Λ' when the filaments are far from each other;

- the combination of both defects results in a significant increase of the porosity ϕ and permeabilities q_0 and q_0' when the filaments are very close to each other. Moreover, an increase of the thermal length Λ' is achieved when the filaments are far from each other.

6

Table II. JCAL parameters relative difference (%) of grooved rods with respect to perfectly cylindrical rods.

Defect	A	ϕ	α_∞	Λ	Λ'	q_0	q_0'
	1.2	5	1	-14	-24	4	4
Grooves	10	0	0	-16	-26	0	0
	25	0	0	-16	-26	0	0

B. Micro grooves

In order to study the effect of the presence of the micro grooves on the acoustic parameters a simple 2D model have been developed. The grooves have not been implemented in a 3D model because of an exceptionally long computation time related to the necessary fine mesh size of the grooves. In the 2D case the REV is shown in Fig. 8(a). In reality, the distribution of grooves is random, their depth cannot be measured precisely. Here, we have considered rods of diameter D equally spaced by a distance $D \times A$ in which periodic grooves are added to the rods surface (see Fig. 8(b) and (c)). Note that fillets on the corners of the grooves are required to respect the MAM surfaces conditions.

Figure 8 shows the dimensions of the geometry, the converged mesh and the visco-inertial MAM velocity field. The latter is used to compute the viscous length Λ. On the one hand, the porosity ϕ, tortuosity α_∞, viscous q_0 and thermal q_0' permeabilities are not affected by the grooves or verry little when the A is close to 1.2. Then their relative variations are 5%, 1%, 4% and 4% respectively. On the other hand, the characteristic lengths Λ and Λ' are impacted by the grooves. Λ is reduced by 16% while Λ' is reduced by 26%. These variations are constant except when A is close to 1.2. The variation of Λ' was expected as its definition is the ratio of the fluid volume to the fluid-skeleton surface[18]. Thus, the presence of grooves leads to the variation of the fluid-skeleton surface without changing the fluid volume except when the rods are very close to each other and the porosity is affected by the grooves. The JCAL parameters variation with respect to the case without grooves are summarized in Table II.

V. EFFECT OF MANUFACTURING DEFECTS ON THE JCAL PARAMETERS: ACOUSTIC EVALUATION

A. Direct comparison between idealized medium and 3D printed sample.

A comparison between the theoretical and the experimental absorption coefficient of two homogeneous samples was made. These samples, idealized by using the geometry as depicted in Fig. 1, are characterized by the JCAL parameters listed on Table III.

Table III. JCAL parameters of homogeneous samples, considering the idealized REV. $D = 400\,\mu\mathrm{m}$.

Sample	A	ϕ	α_∞	$\Lambda(\mu\mathrm{m})$	$\Lambda'(\mu\mathrm{m})$	$q_0(\mathrm{m}^2)$	$q_0'(\mathrm{m}^2)$
1	2	0.51	1.28	217	252	$2,89.10^{-9}$	$4,05.10^{-9}$
2	3.35	0.70	1.16	451	519	$2,04.10^{-8}$	$2,42.10^{-8}$

The simulated and measured absorption coefficients are presented in Fig. 9. As described in [14], the measured absorption is higher than the simulated one and both curves follow the same trend. Still, it can be noted now that the disparity between measured and simulated absorption coefficient is not the unique consequence of acoustic measurement imprecision. It is evidenced that the measured acoustic absorption coefficient of homogeneous samples do not match the simulation and it is clear that the printed geometry differs from the idealized one, which causes important acoustic discrepancies.
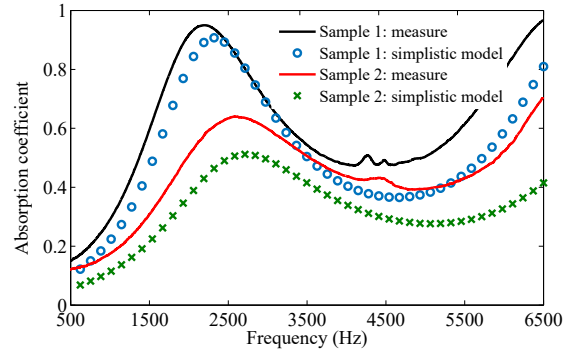

Figure 9. (color online) Absorption coefficient measured (solid lines) and simulated considering the idealized geometry (markers) of homogeneous sample 1 and 2.

B. Fitted model

Finally, three homogeneous samples were used to fit the model predicting the variation of the JCAL parameters with respect to the normalized lattice parameter A. The printer nozzle diameter is equal to $D_n = 400\,\mu\mathrm{m}$. A takes the values 2, 2.5 and 3.35. For each sample, an inverse characterization was performed in order to retrieve the parameters from experiments ($\phi_{fitted}, \alpha_{\infty,fitted}, \Lambda_{fitted}...$) Each parameter bounds are set around the FEM value of the unit cell with elliptical rods section and no pinch. The grooves should significantly reduce the characteristic lengths. Then, during the inverse characterization process, the characteristic lengths can vary between the unit cell values and half of them. The porosity ϕ and tortuosity α_∞ could vary between 80% and 120% of the unit cell value, and

permeabilities q_0 and q'_0 between 70% and 130%. Homogeneous samples with significantly larger A have a low absorption coefficient which complicates their inverse characterization. These types of samples are of small practical interest.

In order to fit the JCAL parameters obtained from inverse characterization, the correction of the elliptical rods section unit cell with no pinch, JCAL prediction, must be:

$$\begin{cases} \phi_{fitted} = \phi + 0.05, \ \phi_{fitted} < 1, \\ \alpha_{\infty,fitted} = \alpha_\infty + 0.05, \\ \Lambda_{fitted} = 0.6 \ \Lambda, \\ \Lambda'_{fitted} = \Lambda', \\ q_{0,fitted} = 0.82 \ q_0, \\ q'_{0,fitted} = 0.80 \ q'_0. \end{cases} \quad (14)$$

Surprisingly, it appears that Λ' did not vary. Moreover, the parameters are simply shifted with respect to the ones predicted by the unit cell, regardless of the filaments spacing.

To validate the corrected predictive model, one homogeneous sample ($A = 1.52$), two bi-layers ($A = [1.5, 3.75]$ and $A = [2, 3]$) and one ten-layers ($A = [1.75, 2, 2.25, ...4]$) samples were printed and simulated by the TMM. It should be noted that some of the considered A are slightly outside the range defined by the three homogeneous samples used for the inverse characterization. Each sample was printed in one step. Figure 10 presents the absorption coefficient measured and predicted on both sides of the multilayer samples. The bi-layer samples are composed of two 15 mm thick layers. The ten-layers sample is composed of ten 3 mm thick layers. It can be observed that the simplistic model without corrections do not fit well the measured absorption coefficients while the corrected model, Eq. (14), is in full agreement with the experimental values. The same observation is made for the homogeneous sample.

C. Accurate prediction model routine

The approach taking into account the impact of the geometry defects is summarized in Fig. 11. It can be applied to other porous materials and to other manufacturing techniques. It consists in simulating the JCAL parameters of the unit cell using the MAM. Experimental geometric and acoustic measurements, including inverse characterization of homogeneous samples, tune the prediction model. Defects that can be simply and accurately described such as elliptical section or filaments pinch should be accounted for in the definition of the unit cell, while complicated or random defects such as grooves are considered by fitting the equivalent fluid parametric model. TMM with the corrected model is applied to mul-
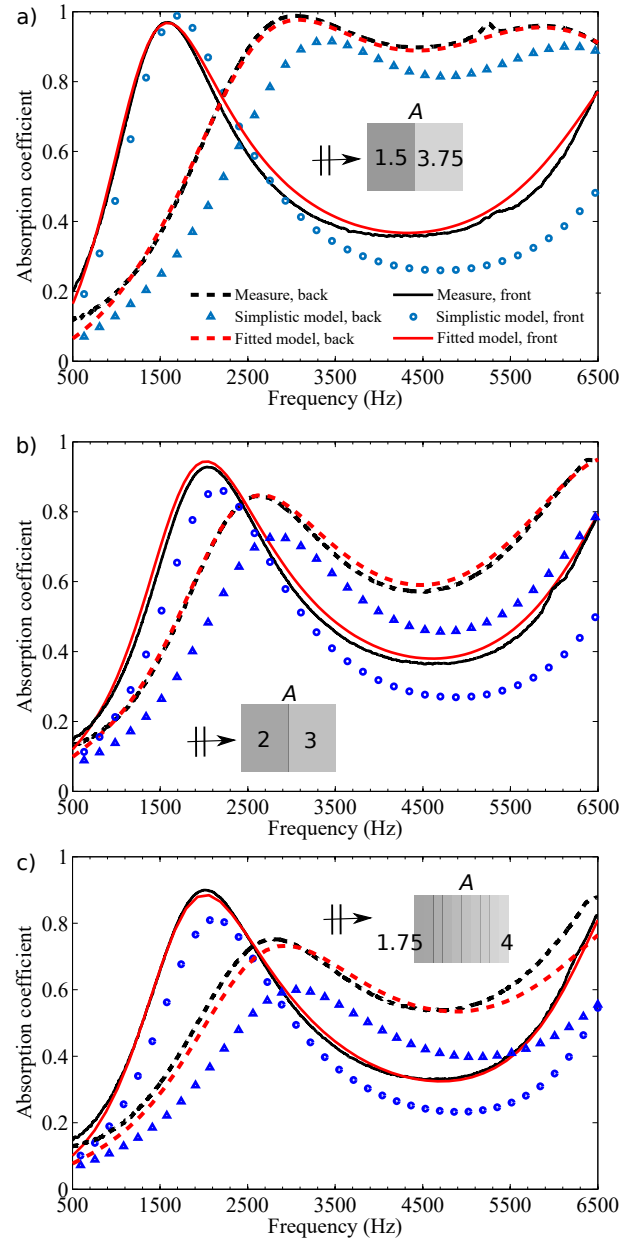

Figure 10. (color online) Absorption coefficient of 30 mm thick multilayers, $D_n = 400 \ \mu$m, samples, measured (black lines) and simulated without considering the defects (blue marks) and simulated by the fitted model (red lines) on both sides. a) $A = 1.5$ and 3.75. b) $A = 2$ and 3. c) $A = 1.75$, 2, 2.25, ...4.

tilayered samples and compared to experimental results in order to validate the routine.

VI. CONCLUSION

In this paper, the discrepancies between an idealized micro-lattice and its actual geometry have been discussed. Considering a simple model enables a rough pre-
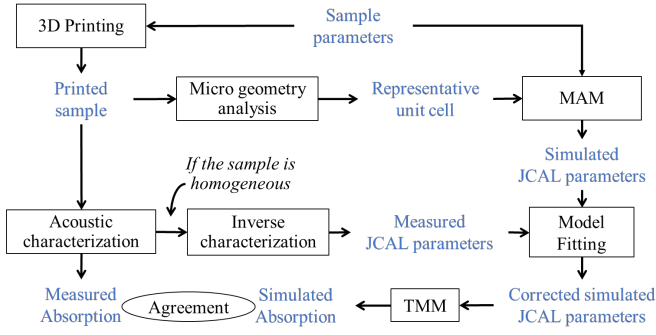
8

Figure 11. Routine diagram.

diction of the acoustic behavior. However, neglecting the micro-geometrical defects such as elliptical section, pinch or nano-rugosity reduce the accuracy of the model. The effect of each defect has been detailed in terms of JCAL parameters. Some of them depend on the filaments spacing, especially when it is very small. An experimental fitting routine based on prior knowledge of the parameters scopes can easily be performed leading to an increased precision of the predictive model.

This article focused on FDM 3D printed micro-lattice. Yet, micro-geometrical defects are not specific to this porous material or this additive manufacturing technique. The routine leading to an accurate prediction model can be applied to other porous materials made by other 3D printing processes such as stereolithography or selective laser melting.

Moreover, micro-geometrical defects are most probably device-dependent. In other words, two synchronized printers of the same model, might not manufacture samples having the same acoustic parameters. In a similar fashion, the micro-geometrical defects might dependent on device wear.

REFERENCES

[1] X. Cai, Q. Guo, G. Hu, and J. Yang, "Ultrathin low-frequency sound absorbing panels based on coplanar spiral tubes or coplanar Helmholtz resonators," Applied Physics Letters **105**, 121901 (2014).

[2] C. Jiang, D. Moreau, and C. Doolan, "Acoustic Absorption of Porous Materials Produced by Additive Manufacturing with Varying Geometries," , 8 (2017).

[3] Z. Liu, J. Zhan, M. Fard, and J. L. Davy, "Acoustic properties of a porous polycarbonate material produced by additive manufacturing," Materials Letters **181**, 296–299 (2016).

[4] M. D. Guild, V. M. Garcia-Chocano, W. Kan, and J. Sánchez-Dehesa, "Acoustic metamaterial absorbers based on confined sonic crystals," Journal of Applied Physics **117**, 114902 (2015), arXiv: 1405.7200.

[5] Z. Liu, J. Zhan, M. Fard, and J. L. Davy, "Acoustic properties of multilayer sound absorbers with a 3d printed micro-perforated panel," Applied Acoustics **121**, 25–32 (2017).

[6] E. R. Fotsing, A. Dubourg, A. Ross, and J. Mardjono, "Acoustic properties of periodic micro-structures obtained by additive manufacturing," Applied Acoustics **148**, 322–331 (2019).

[7] X. Cai and J. Yang, "Sound Absorption by Acoustic Microlattice with Optimized Pore Configuration," , 21.

[8] M. D. Guild, M. Rothko, C. F. Sieck, C. Rohde, and G. Orris, "3d printed sound absorbers using functionally-graded sonic crystals," The Journal of the Acoustical Society of America **143**, 1714–1714 (2018).

[9] J.-L. Auriault, C. Boutin, and C. Geindreau, *Homogenization of coupled phenomena in heterogenous media* (2009) oCLC: 733729827.

[10] C.-Y. Lee, M. J. Leamy, and J. H. Nadler, "Numerical Calculation of Effective Density and Compressibility Tensors in Periodic Porous Media: A Multi-Scale Asymptotic Method," (Boston, 2008) p. 6.

[11] R. Venegas and O. Umnova, "On the influence of the micro geometry on sound propagation through periodic array of cylinders," The Journal of the Acoustical Society of America **123**, 3142–3142 (2008).

[12] S. Y. Song, X. H. Yang, F. X. Xin, S. W. Ren, and T. J. Lu, "Modeling of roughness effects on acoustic properties of micro-slits," Journal of Physics D: Applied Physics **50**, 235303 (2017).

[13] J. A. Kulpe, C.-Y. Lee, and M. J. Leamy, "Computation of acoustic absorption in media composed of packed microtubes exhibiting surface irregularity," The Journal of the Acoustical Society of America **130**, 826–834 (2011).

[14] Zielinski, "Pore-size effects in sound absorbing foams with periodic microstructure: modelling and experimental verification using 3d printed specimens," (2016).

[15] S. Deshmukh, H. Ronge, and S. Ramamoorthy, "Design of periodic foam structures for acoustic applications: Concept, parametric study and experimental validation," Materials & Design **175**, 107830 (2019).

[16] D. Lafarge, P. Lemarinier, J. Allard, and V. Tarnow, "Dynamic compressibility of air in porous structures at audible frequencies," J. Acoust. Soc. Am. **102**, 1995–2006 (1997).

[17] M. Niskanen, J.-P. Groby, A. Duclos, O. Dazel, J. C. Le Roux, N. Poulain, T. Huttunen, and T. Lahivaara, "Deterministic and statistical characterization of rigid frame porous materials from impedance tube measurements," The Journal of the Acoustical Society of America **142**, 2407–2418 (2017).

[18] J.-F. Allard and N. Atalla, *Propagation of sound in porous media: modelling sound absorbing materials*, 2nd ed. (Wiley, Hoboken, N.J, 2009).